AGU PUBLICATIONS

JGR

Journal of Geophysical Research: Space Physics

RESEARCH ARTICLE
10.1002/2013JA018955

Key Points:
- GWs propagation direction in January 2006 was related with SSW
- Momentum fluxes are modulated strongly by diurnal and semi-diurnal tides
- the tide is possibly amplifed (suppressed) during equinoxes (solstices) by GWs

Correspondence to:
X. Dou,
dou@ustc.edu.cn

Citation:
Tang, Y., X. Dou, T. Li, T. Nakamura, X. Xue, C. Huang, A. Manson, C. Meek, D. Thorsen, and S. Avery (2014), Gravity wave characteristics in the mesopause region revealed from OH airglow imager observations over Northern Colorado, *J. Geophys. Res. Space Physics*, *119*, 630–645, doi:10.1002/2013JA018955.

Received 23 APR 2013
Accepted 26 DEC 2013
Accepted article online 2 JAN 2014
Published online 31 JAN 2014

Gravity wave characteristics in the mesopause region revealed from OH airglow imager observations over Northern Colorado

Yihuan Tang[1], Xiankang Dou[1], Tao Li[1], Takuji Nakamura[2], Xianghui Xue[1], Can Huang[1], Alan Manson[3], Chris Meek[4], Denise Thorsen[5], and Susan Avery[6]

[1]CAS Key Laboratory for Geospace Environment, School of Earth and Space Sciences, University of Science and Technology of China, Hefei, China, [2]National Institute of Polar Research, Tachikawa, Japan, [3]School of Earth and Environmental Science, City University of New York, New York, New York, USA, [4]Institute of Space and Atmospheric Studies, University of Saskatchewan, Saskatoon, Saskatchewan, Canada, [5]Department of Electrical and Computer Engineering, University of Alaska Fairbanks, Fairbanks, Alaska, USA, [6]Woods Hole Oceanographic Institution, Woods Hole, Massachusetts, USA

Abstract Using 5 years of all-sky OH airglow imager data over Yucca Ridge Field Station, CO (40.7°N, 104.9°W), from September 2003 to September 2008, we extract and deduce quasi-monochromatic gravity wave (GW) characteristics in the mesopause region. The intrinsic periods are clustered between approximately 4 and 10 min, and many of them are unstable and evanescent. GW occurrence frequency exhibits a clear semiannual variation with equinoctial minima, which is likely related to the seasonal variation of background wind. The anomalous propagation direction in January 2006, with strong southward before major warming starting in 21 January and weak southward propagation afterward, was most likely affected by stratospheric sudden warming. The momentum fluxes show strongly anticorrelated with the tides, with ~180° out of phase in the zonal component. While in the meridional component, the easterly maximum occurred approximately 2–6 h after maximum easterly tidal wind. However, the anticorrelations are both weakest during the summer. The dissipating and breaking of small-scale and high-frequency GW's components could have a potential impact on the general circulation in the mesopause region.

1. Introduction

Gravity waves (GWs) are believed to play an important role in driving the general circulation in the mesosphere and lower thermosphere (MLT) region through deposition of their momentum and energy into the mean flow [*Vincent*, 1984; *Hamilton*, 1996; *Fritts and Alexander*, 2003]. GWs are mostly generated in the lower atmosphere and propagate upward with exponential amplitude growth due to the exponential decrease in air density. The GWs tend to become unstable or break via either Kelvin-Helmholtz or Rayleigh-Taylor instabilities if a critical layer is encountered or the amplitude grows sufficiently large. As a result, the GWs will deposit their momentum and energy into the mean flow and thus cause the variability of the background temperature and wind [*Fritts and Rastogi*, 1985; *Li et al*., 2005]. The basic mechanisms of the breaking of GW have been presented by *Fritts* [1984]. However, studies of the GW parameterization are even more important to the development of general circulation models (GCMs). An all-sky nightglow imager provides a very effective way to observe the temporal and spatial characteristics of GWs over the long term.

In recent decades, the all-sky airglow imager has been applied at many sites to detect high-frequency, quasi-monochromatic GWs with periods that are commonly shorter than 1 h and are believed to contribute 70% of the total GW momentums in the mesopause region as revealed by early radar observations [*Fritts and Vincent*, 1987]. *Tang et al*. [2005] applied a two-dimensional (2-D) cross periodogram to two consecutive Doppler-shifted time-differenced (TD) OH images to identify wave components and intrinsic wave parameters, as well as to estimate the momentum flux using a model developed by *Swenson and Liu* [1998]. Typical horizontal wavelengths of GWs observed using the airglow imager in the MLT are approximately 30 km and range from 20 to 100 km. Their phase speeds range from ~30 to 100 m s^{-1}, and the intrinsic wave periods range from 5 min to several dozen minutes with a typical value of 10 min [*Taylor et al*., 1997; *Stockwell and Lowe*, 2001a; *Ejiri et al*., 2003; *Tang et al*., 2005; *Suzuki et al*., 2007; *Nielsen et al*., 2009]. The average momentum flux is approximately 5 to 15 m^2 s^{-2} [*Tang et al*., 2005; *Suzuki et al*., 2007; *Li et al*., 2011a].

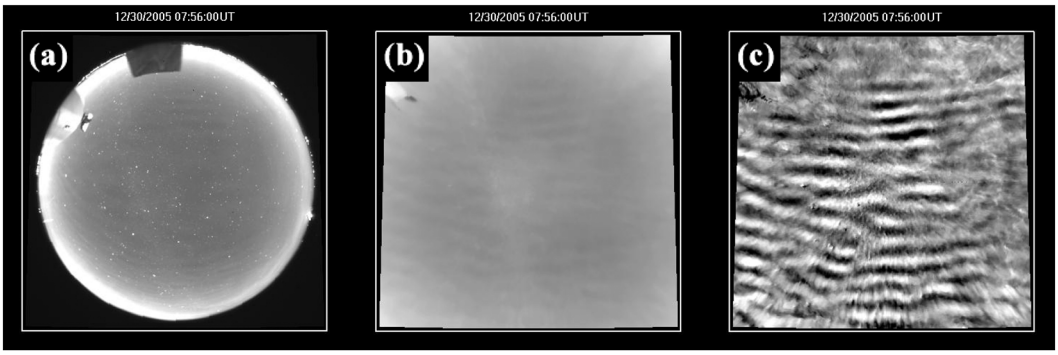

Figure 1. OH image processing. (a) Example of raw all-sky OH airglow images at 0756 UT obtained at Yucca Ridge Field Station on 30 December 2005. (b) Same as Figure 1a except that it was a corrected intensity count projected onto the geographical grid with a size of 400 km × 400 km. The NNW-SSE structure in the center of the images is the Milky Way. (c) Same as Figure 1b, except that the Milky Way and undisturbed counts were removed.

The propagation of GWs observed using OH imagers shows a clear seasonal dependence, with prevailing eastward and poleward propagation in the summer and equatorward propagation in the winter [*Nakamura et al*., 1999; *Hecht et al*., 2001; *Ejiri et al*., 2003; *Tang et al*., 2005; *Dou et al*., 2010; *Li et al*., 2011a]. It is proposed that the dominant zonal propagation directions in the summer are most likely due to mean wind filtering [*Taylor et al*., 1993; *Stockwell and Lowe*, 2001b], and the major meridional propagation directions in the winter are likely caused by ducting condition [*Walterscheid et al*., 1999; *Hecht et al*., 2001; *Suzuki et al*., 2004] and wave source location [*Nakamura et al*., 2003]. Furthermore, the propagation direction of GWs also shows significant latitudinal variations. Doppler shifting by the local background wind might also contribute to GWs' propagation direction preferences through the modification of vertical wavelengths of GWs by the background wind [*Fritts and Wang*, 1991; *Li et al*., 2011a].

This paper uses the long-term OH imager observations at Yucca Ridge Field Station, CO (40.7°N, 104.9°W), and MF radar wind measurements at Platteville, CO, to study the GW characteristics and momentum flux in the MLT over Northern Colorado. Based on the analysis results, we also discuss the correlation between the seasonal variations of the GWs' propagation direction, their momentum flux, and the background wind.

2. Data and Methodology

The all-sky OH airglow imager has been located at Yucca Ridge Field Station, CO (40.7°N, 104.9°W), since September 2003 [*Nakamura et al*., 2005]. It has a 25 mm diameter low-pass filter with a cutoff feature at 795 nm, a fish-eye lens with a view field of 180°, and an air-cooled CCD (Charge Coupled Device) camera with 1024 × 1024 pixels. The images are binned to 512 × 512 pixels to increase the signal-to-noise ratio. The integration time and temporal resolution of the OH images are 100 s and 120 s, respectively. The MF radar (2.219 MHz) at Platteville, CO (40.2°N, 104.7°W), provided almost continuous wind information around the OH layer region (79–94 km) from 2003 to 2008. The wind data are hourly means with a vertical resolution of 3 km for further analysis. MF radar winds are generally smaller than the winds observed using the meteor radar, especially in winter [*Jacobi et al*., 2008]. This would influence some of the calculated values, partly but not significantly.

2.1. Image Processing

Figure 1a shows an example of an all-sky OH image. The image contains information with various effects, including small-scale GWs. To extract small-scale (~20−100 km) GWs, we need to perform further analysis on the image.

First, the dark counts were removed by subtracting the dark image observed every 30 min from the raw images. Then, the dark subtracted images were calibrated with the known stars' locations, such as the Polaris that was circled around by other stars. Then, bright stars were attenuated from images through a median filter with widths of 20 × 20 pixels [*Garcia et al*., 1997; *Coble et al*., 1998; *Suzuki et al*., 2007]. This method is effective at attenuating contaminations from stars and other spike-like structures in the image.

Second, due to the van Rhijin effect and lens vignetting of the fish-eye lens, the airglow intensity $I_{\text{true}}(\theta)$ observed from the ground is not uniform at different zenith angles, even though the airglow emission is spatially uniform. The observed airglow intensity is also affected by atmospheric extinction, due to atmospheric absorption and scattering in the line of sight. The relation between the apparent airglow intensity $I(\theta)$ at zenith angle θ from the ground and the true airglow intensity $I_{\text{true}}(\theta)$ at the emission layer is given by the equations [*Kubota et al*., 2001]:

$$I(\theta) = I_{\text{true}}(\theta)\cdot 10^{-0.4aF(\theta)} = V(\theta)\cdot 10^{-0.4aF(\theta)}\cdot I(0) \tag{1}$$

$$V(\theta) = \left[1 - \left(\frac{R_E}{R_E + H_{\text{OH}}}\right)\sin^2\theta\right]^{-\frac{1}{2}} \tag{2}$$

and

$$F(\theta) = \left[\cos\theta + 0.15\left(93.885 - \frac{180}{\pi}\cdot\theta\right)^{-1.153}\right]^{-1} \tag{3}$$

where $I(0)$ is the intensity at zenith, R_E and H_{OH} are the earth radius and OH airglow layer altitude of approximately 87 km, respectively, $V(\theta)$ is the van Rhijin correction factor, a is atmospheric extinction coefficient, and $F(\theta)$ is an empirical equation. The above-mentioned effects were corrected by fitting a reasonable factor a, whose value is approximately 0.38 in most cases. An empirical correction technique provided by *Hecht et al*. [2005] is also very appropriate if observational time is enough every night.

Third, because a filter with a broad-pass OH band was used in our imager, the background contamination counts, including the light scattered by dust from urban areas and from the atmospheric continuum emission, needed to be subtracted from the raw image. *Swenson and Mende* [1994] deduced that the background counts accounted for approximately 30% of the total OH image signal. Measurement by Spectral Airglow Temperature Imager (SATI) in Shigaraki, Japan, [*Suzuki et al*., 2007] showed that the contribution of the background contamination was comparable to that deduced by *Swenson and Mende* [1994]. The OH imager at Yucca Ridge Field Stations is fundamentally similar to Suzuki's, so we also assume 30% of raw counts in each pixel of the images to be the background counts.

Finally, the corrected OH images were mapped into the geographical coordinates with a size of 400×400 km in 512×512 grids by assuming the OH airglow layer altitude at 87 km, as shown in Figure 1b. Then, we calculated the mean OH pixel intensity $\bar{I}_{\text{OH}}$ for the whole night. To remove undisturbed intensity $\bar{I}_{\text{OH}}$ and detrend the images, we obtained time-differenced (TD) OH images based on the differences between two sequential images using the method developed by *Tang et al*. [2005]. To damp some wave-like structures, such as "ripple," traveling with background wind and having intrinsic phase speed close to zero, Doppler-shifting correction by background wind needed to be applied before taking the TD images. This process may also suppress part of low-frequency waves but does not impact on high-frequency waves significantly which are the concerned in this paper. We grouped three consecutive images and used the second image as a base. For the first (third) image in the sequence, the pixels were shifted toward (against) the wind by the same distance as the wind traveled in the time interval between two images. Then the two TD images were normalized by mean OH pixel intensity $\bar{I}_{\text{OH}}$. An example of the final TD images obtained is shown in Figure 1c.

2.2. Wave Detection and Identification

After the above procedures, a group of two OH intensity disturbed images were generated from three sequential images. Thus, the gravity wave parameters can be determined every 6 min. Using spectral analysis techniques, we identified gravity waves from the TD images and determined their zonal and meridional wave numbers (k,l), horizontal wavelengths λ_h, intrinsic frequency ω_i, intrinsic phase speeds c, and intensity perturbation $I'_{\text{OH}}/\bar{I}_{\text{OH}}$.

To further attenuate the effects of large-scale (larger than ~100 km) intensity perturbations, such as those by the Milky Way, we divided every TD image into 9 separate but overlapping parts as shown in Figure 2. Then, a two-dimensional (2-D) prewhitening filter, introduced by *Coble et al*. [1998], and a 2-D Hanning window were applied to each part of the images before the Fourier analysis. Then, the 2-D fast Fourier transform (FFT) was applied to every two related parts of two TD images to acquire two periodograms and a cross periodogram.

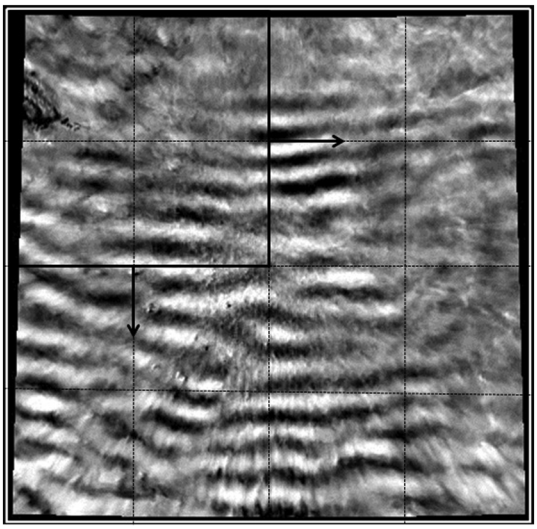

Figure 2. Illustration of nine separate but overlapping parts of a TD image. The arrows represent the moving directions of the analysis window.

Let $X_1(k,l)$ and $X_2(k,l)$ denote their FFTs, where k and l represent the wave numbers in the zonal and meridional directions, respectively. The cross periodogram $Y_{12}(k,l)$ can be represented as

$$Y_{12}(k,l) = X_1(k,l)X_2^*(k,l), \tag{4}$$

where the asterisk designates the complex conjugate. The squared magnitude of the cross periodogram

$$|Y_{12}(k,l)|^2 = |X_1(k,l)|^2|X_2(k,l)|^2, \tag{5}$$

is then used to identify common wave components. A typical periodogram spectrum is shown in Figure 3. Propagation direction and zonal and meridional wave numbers are determined from the peak position of the spectra. Due to the 180° ambiguity for the FFT analysis, the wave propagation direction needs to be solved by calculating the phase θ of the cross-power spectrum $Y_{12}(k,l)$. The positive phase peak represents the real wave propagation direction.

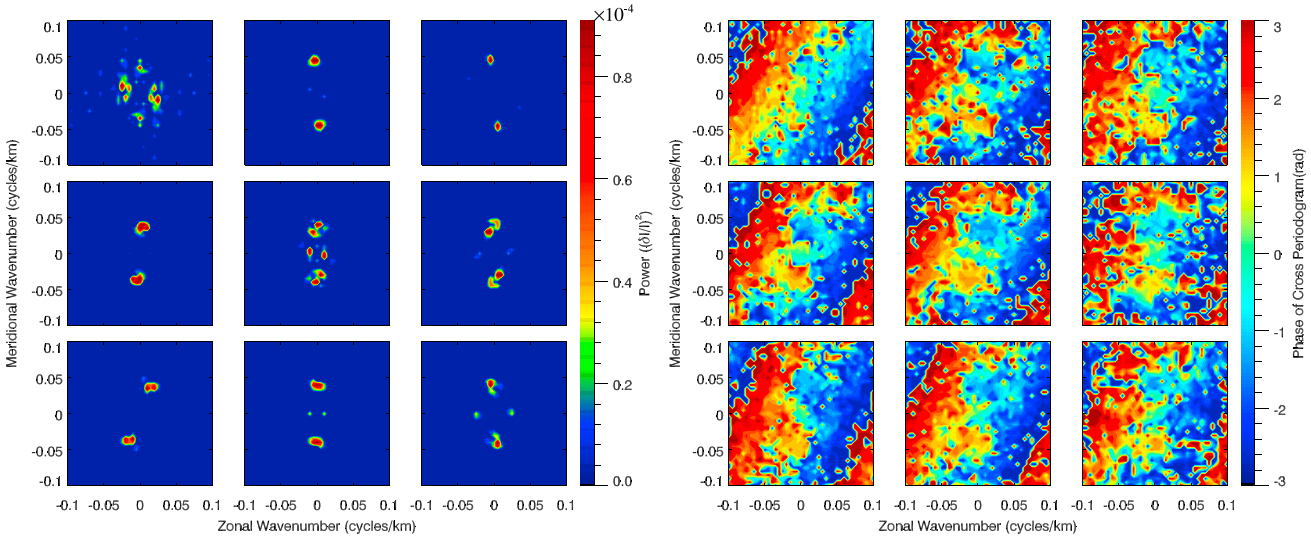

Figure 3. Cross periodogram spectrum at 0754–0758 UT, 30 December 2005, Northern Colorado, CO. (left) Power of the cross periodogram. (right) Phase of the cross periodogram.

To estimate the intensity perturbation $I'_{OH}/\bar{I}_{OH}$ from spectra, the peak magnitude of the cross periodogram should be corrected because of the magnitude modulation of the Hanning window. Through assumption of ideal sinusoidal waves, the correction was made using the method introduced by *Ming and Kang* [1996]. The 2-D situation was deduced from their method:

$$A = \frac{\pi\Delta\lambda_k}{\sin(\pi\Delta\lambda_k)} \cdot \frac{\pi\Delta\lambda_l}{\sin(\pi\Delta\lambda_l)} \cdot 2\left(1-\Delta\lambda_k^2\right)\cdot 2\left(1-\Delta\lambda_l^2\right)\cdot Y_{k,l}, \tag{6}$$

where A is the corrected peak amplitude, $Y(k,l)$ is the apparent peak amplitude in the cross periodogram spectrum, and k and l are indices of zonal and meridional direction, respectively. The wave number correction factor $\Delta\lambda_k$ is defined as

$$\Delta\lambda_k = \begin{cases} \dfrac{Y_{k+1,l}}{Y_{K+1,l}+Y_{k,l}} & \left(Y_{k+1,l} \geq Y_{k-1,l}\right) \\ \dfrac{-Y_{k-1,l}}{Y_{k,l}+Y_{k-1,l}} & \left(Y_{k+1,l} \leq Y_{k-1,l}\right) \end{cases}, \tag{7}$$

and $\Delta\lambda_l$ is defined similarly. $Y_{k+1,l}$ and $Y_{k-1,l}$ are the amplitudes of two spectral lines near the main lobe in the k direction.

The estimated value of the perturbed intensity above from TD images must be mapped to a corresponding value in the original images. By modeling an ideal sinusoidal wave, the ratio between the Doppler-shifted TD wave amplitude A_{TD} and the original wave amplitude A_o is deduced by *Tang et al.* [2005],

$$\frac{A_{TD}}{A_o} = 2\left|\sin\left(\frac{\omega_i \Delta t}{2}\right)\right|, \tag{8}$$

where Δt is the time interval between two successive images.

To distinguish the peaks caused by gravity waves from those caused by noise or other structures, several criteria were adopted as follows:

1. Individual gravity waves should have a power greater than 10% of the total spectrum.
2. Intensity amplitude is greater than 0.5% but less than 10%.
3. An intensity amplitude larger than 10% might be caused by cloud or other strong structures; horizontal wavelengths are more than 12 km but less than 100 km.

Waves with horizontal wavelengths of more than 100 km might be caused by the Milky Way, and waves with horizontal wavelengths of less than 12 km are too small to be observed by the airglow imager, considering the thickness of the OH airglow layer [*Swenson et al.*, 2000].

Up to 9 GW events were deduced, in which some may be caused by one dominant GW. From a group of two TD images, we usually found one dominant wave event that primarily contributed to momentum flux. In these events, we defined the gravity waves as one dominant wave, if the difference of at least 3 GW events' propagation directions was less than 30° or both the change rates of horizontal wavelength and frequency were within 20%. Otherwise, we defined that there was no wave event. Through this process, the parts covered by cloud are mostly eliminated from the total 9 parts of TD images.

2.3. Momentum Flux Calculation

The GW's momentum flux per unit mass is defined as the covariance of horizontal and vertical wind perturbations. We use the *Swenson and Liu* [1998] model to estimate momentum flux for a monochromatic gravity wave

$$F_M = \frac{g^2}{N^2}\cdot\frac{k}{m\cdot \mathrm{CF}^2}\cdot\left(I'/\bar{I}\right)^2 \quad \left(m^2\cdot s^{-2}\right), \tag{9}$$

where g is the acceleration of gravity, N is the buoyancy (Brunt-Vaisala) frequency, $k = 2\pi/\lambda_h$ is the horizontal wave number, λ_h is the horizontal wavelength, $m = 2\pi/\lambda_z$ is the vertical wave number, λ_z is the vertical wavelength, CF is the cancellation factor, and $I'/\bar{I}$ is the relative intensity perturbation.

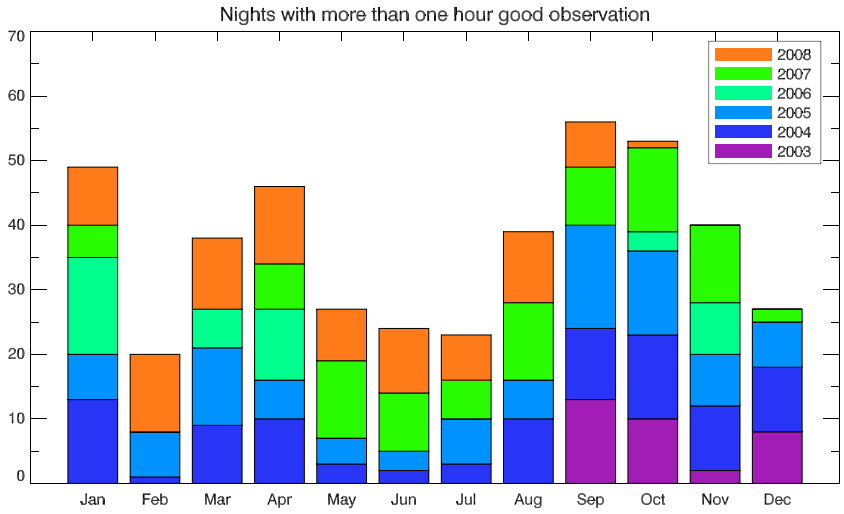

Figure 4. Distribution of nights with good observation condition and enough observation time.

The cancellation factor CF connects the perturbations of temperature and OH airglow intensity as $T'/\overline{T} = (I'/\overline{I})/CF$, where $\overline{T}$ is the undisturbed temperature. It is approximated by the analytic expression [*Swenson and Liu*, 1998]

$$\mathrm{CF} = 3.5 - (3.5 - 0.01)\exp\left[-0.0055(\lambda_z - 6\ \ \mathrm{km})^2\right]. \tag{10}$$

For small λ_z, CF decreases rapidly as the cancelation effect increases, so it is difficultly detected by airglow imager. But on the other side, for the waves with $\lambda_z < 12$ km, small errors in airglow intensity perturbation divided by small CFs would introduce large errors in inferred momentum flux according to equations (9) and (10), due to their strong cancelations in the airglow layer (small CFs). Thus, the waves with $\lambda_z < 12$ km are excluded in the calculation of momentum flux.

The vertical wave number m is calculated through the dispersion relation [*Alexander*, 1998]

$$m^2 = \frac{N^2 - \omega^2}{\omega^2 - f^2}k^2 - \frac{1}{4H^2}, \tag{11}$$

where ω is the intrinsic frequency, f is the inertial frequency, and H is the scale height. Near 90 km, the scale height is ~7 km. The squared buoyancy frequency, N^2, is defined as

$$N^2 = \frac{g}{T}\left(\frac{\mathrm{d}T}{\mathrm{d}z} + \frac{g}{c_p}\right), \tag{12}$$

where c_p is the specific heat at constant pressure and the temperature profiles are calculated from the NRLMSISE-00 model [*Picone et al.*, 2002]. N^2 is obtained by averaging the airglow layer with a thickness of 10 km centered at 87 km.

3. Results and Discussion

There are 451 nights of observation from September 2003 to September 2008 with at least 1 h of favorable time with no clouds. The number of nights with favorable observation conditions for each month is summarized in Figure 4. It is obvious that the number of favorable nights observed in summer is less than that in other months because of weather conditions. In addition, in most years, there is a lack of some months with favorable conditions except 2004 and 2005. However, for all of the months, even in the summer and in February, there are at least 20 nights and enough observation time with favorable condition, so the statistics of GW characteristics are reliable.

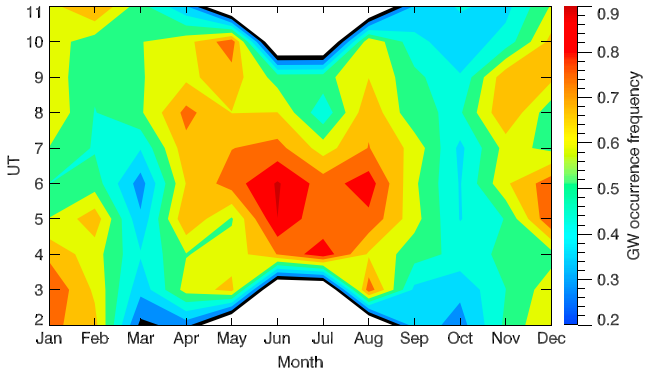

Figure 5. GW occurrence frequency as function as month and universal time.

3.1. Wave Characteristics

Each sequence of three raw images with a time interval of 2 min was analyzed as a group. Using a definition similar to *Li et al*. [2011a], a dominant wave persisting for at least 6 min was considered a wave event. Analysis of these images reveals a total of 9532 waves with a lifetime that is longer than 6 min. We count only one wave event per group, which is different from the method used by *Li et al*. [2011a]. The wave occurrence frequency is defined as a ratio of the number of persistent waves to the number of observation intervals.

Figure 5 shows the distribution of wave occurrence frequency with time and month. Although the mean occurrence frequency of 56% is less than the occurrence frequency (more than 80%) in our previous studies [*Dou et al*., 2010] with waves identified individually and manually, the results show a much stronger seasonal dependence. GW occurrence frequency exhibits a clear semiannual variation with solstitial maxima and equinoctial minima, which is consistent with previous imager studies [e.g., *Li et al*., 2011a] and radar measurements [e.g., *Nakamura et al*., 1996]. In summer the occurrence frequency reaches maxima of more than 65%, especially before midnight between 0400 and 0700 UT (local time is 7 h behind universal time) with occurrence frequencies higher than 75%, while fewer waves are observed from September to November and in March, with occurrence frequency lower than 50%. Many factors may influence on GW activity. *Nakamura et al*. [1996] thought the background wind variation, such as semiannual oscillation, mesospheric semiannual oscillation, and other wind variations, would strongly affect the GW activity. *Gardner and Liu* [2007] reported that temperature and wind variances show strong semiannual oscillations also with minima at the equinoxes based on lidar observation at Starfire Optical Range. *Li et al*. [2011a] analyzed the influence of convective activity on GW occurrence and found the peak of wave occurrence season actually corresponds to a time of less convection and convective precipitation at Maui. It is also noticed that tidal amplitude shows a semiannual variation but with maxima at the equinoxes and might also be one of the factors influencing GW activity. Further analysis on the seasonal variation of GW occurrence frequency will be performed in future research.

Figure 6 shows the distributions of extracted or derived GWs parameters in Colorado, including horizontal wavelength (Figure 6a), vertical wavelength (Figure 6b), intrinsic phase speed (Figure 6c), observed phase speed (Figure 6d), intrinsic period (Figure 6e), and observed period (Figure 6f). A summary of the results from several previous imaging studies on short-period GWs worldwide is illustrated in Table 1.

Figure 6a shows that the majority of the quasi-monochromatic wave events exhibited horizontal wavelengths in a range of 20–60 km with a mean value of 40 km and a peak of 30 km, which is consistent with previous studies shown in Table 1. The spatial resolution and scope of airglow imagers influence the range of observed horizontal wavelength to some extent. The peak horizontal wavelengths in the spectra of observed GWs are likely generated by convection [*Lane and Moncrieff*, 2008]. Figure 6b shows that vertical wavelength ranges from 10 to 60 km centered approximately 20–30 km. In addition to mean flow filtering, GWs are filtered by imager observation because of the thickness of the OH layer (~10 km). Meanwhile, the shorter vertical wavelength (smaller cancelation factor) corresponds to stronger cancelation in airglow intensity perturbation observed on the ground. Thus, the percentage of waves decreases with decreasing vertical wavelength. However, *Hu et al*. [2002] reported that many GWs with horizontal wavelength larger than

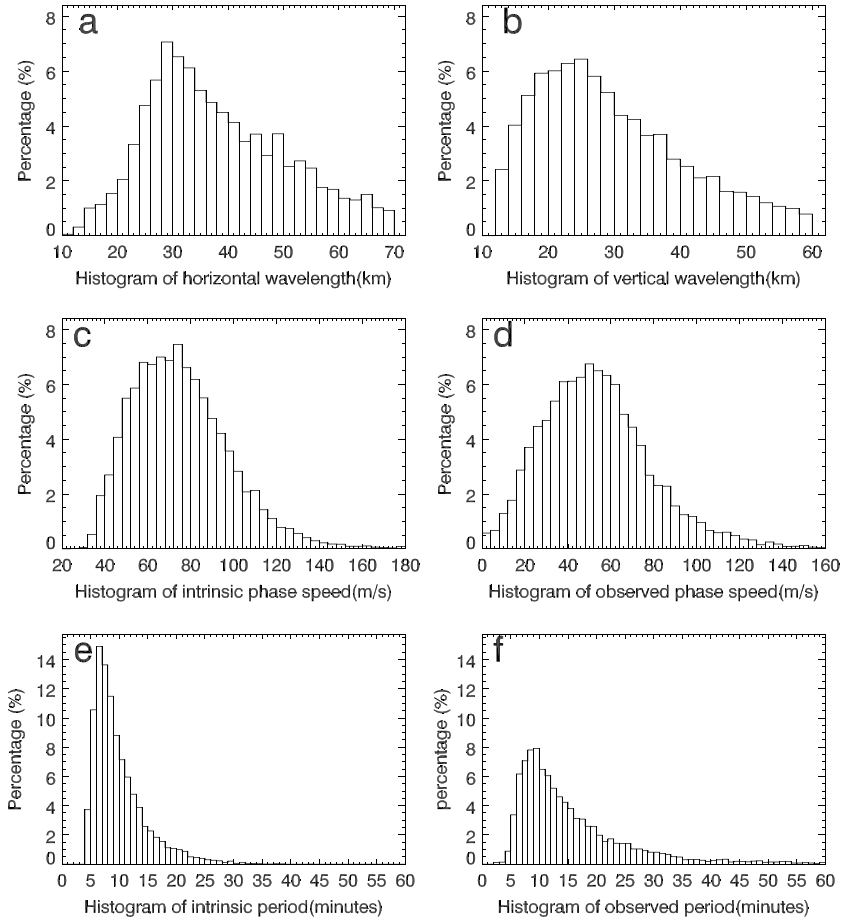

Figure 6. Distributions of extracted or derived GWs parameters. (a) Horizontal wavelength histogram. The bin width is 2 km. (b) Histogram of vertical wavelength. The bin width is 2 km. (c) Histogram of intrinsic phase speed. The bin width is 4 m s^{-1}. (d) Observed phase speed histogram with the bin width 4 m s^{-1}. (e) Intrinsic wave period histogram. The bin width is 1 min. (f) Observed wave period histogram with the bin width 1 min.

Table 1. Summary Results of Previous Mostly Imaging Studies on Short-Period GWs Worldwide

Observation Site	Data Duration (months)	λ_h (km)	c (m/s)	T (min)	Observed Propagation Direction	Reference
Rikubetsu, Japan 44°N	12	21–27	20–50	11	N-NE during summer turning to west during winter.	*Ejiri et al.* [2003]
Ontario, Canada 42–43°N	5 (May–Sep)	25	45	10	N-NE during summer and west during winter.	*Stockwell and Lowe* [2001a]
Peach Mountain, MI, USA 42°N	14	N/A	N/A	N/A	Preferential eastward propagation.	*Wu and Killeen* [1996]
Urbana, IL, USA 40°N	15	20–30	50	8	Poleward during spring and summer. No preference during autumn and winter.	*Hecht et al.* [2001]
Nederland, CO, USA 40°N	3 (Apr–May)	N/A	24	N/A	Mainly north and east propagation.	*Taylor et al.* [1993]
Xinglong, China, 40°N	12	22	48	8	NE during summer and SW in winter	*Li et al.* [2011a]
Shigaraki, Japan 35°N	12	21–27	20–50	11	N-NE during summer and SW during winter.	*Nakamura et al.* [1999] *Ejiri et al.* [2003]
Maui, HI, USA 20°N	60	~25	~50	<10	Mainly north during summer, SW-W during winter, and east during spring and autumn.	*Li et al.* [2011a]
Alcantara, Brazil 2°S	3 (Sep–Oct)	24	48	8	N-E during late spring and early summer.	*Taylor et al.* [1997]
Tanjungsari, Indonesia 7°S	12	13–45	37–75	9	Preferential poleward propagation.	*Nakamura et al.* [2003]
Darwin, Australia 12°S	11	30–50	30–60	15	Poleward during summer and both poleward and equatorward during winter.	*Suzuki et al.* [2004]
Cachoeira Paulista, Brazil 23°S	13	23	26	15	SE during summer and NW during winter.	*Medeiros et al.* [2003]
Adelaide, Australia 35°S	10	N/A	N/A	N/A	Poleward during summer and equatorward during winter.	*Walterscheid et al.* [1999]
Halley, Antarctica 76°S	24	25	52	10	Mainly east during spring, NW during autumn, and south during the midwinter.	*Nielsen et al.* [2009]

100 km or vertical wavelength less than 20 km were observed using lidar observation at Starfire Optical Range, NM, which is mainly because the spectrum window of GW observed by lidar is different than that observed by airglow imager.

The intrinsic phase speeds shown in Figure 6c exhibit a more symmetric distribution ranging from 20 to 180 m s^{-1} with typical values of 50–90 m s^{-1} and an average value of 75 m s^{-1}. Intrinsic phase speeds vary as GWs propagate through the mean flow. Thus, compared with the intrinsic phase speeds, the observed phase speeds (the phase speed relative to the ground observer) exhibit a similar distribution but approximately 20 m s^{-1} (the magnitude of background wind) lower than intrinsic phase speeds. This fact indicates that the majority of GWs propagate against background wind. The minority of waves with observed phase speeds close to zero were possibly mountain waves or ripples [*Li et al*., 2011b]. These will need further analysis in the future.

In Figure 6e, the histogram plot of intrinsic wave period shows that short-period waves dominate the distribution with a relatively sharp peak of 7 min and an average value of 10 min. Out of the total, more than 88% of GWs events have an intrinsic period shorter than 15 min. High-frequency GWs with short horizontal wavelength are favored in OH imager observations because they tend to have longer vertical wavelengths and suffer little cancelation effect. Figure 6f presents the histogram of observed period, which shows a broader distribution mainly ranging from 7 to 20 min. This also indicates that the majority of GWs tend to propagate against the background wind so that the GWs are Doppler shifted toward shorter intrinsic period. Likewise, *Hu et al*. [2002] reported low-frequency GWs with wave periods ranging from a few hours to approximately 20 h with a peak value of 10 h. However, high-frequency GWs with periods mainly shorter than 1 h are believed to contribute 70% of the total GW momentum in the mesopause region [*Fritts and Vincent*, 1987] and thus have a bigger impact on mesospheric forcing and transport when they dissipate or break.

Most of the characteristics of GWs, such as horizontal wavelength, vertical wavelength, wave period, and phase speed, do not vary significantly with season, but the propagation direction does. GW propagation directions vary significantly with season and background wind as shown in Figure 7. GWs mainly tend to propagate in meridional directions at midlatitude Yucca Ridge Field Station, while the minority of GWs travel in zonal directions. Stronger wave filtering in the zonal direction by the mean flow in the stratosphere and the lower mesosphere will suppress or block the zonal propagations of GWs [*Taylor et al*., 1993; *Stockwell and Lowe*, 2001b], while the predominate meridional preferences are mainly caused by wave ducting condition and north-south wave sources (such as an equatorial tropospheric convective source) that allow GWs to propagate upward to the mesosphere [*Walterscheid et al*., 1999; *Hecht et al*., 2001; *Suzuki et al*., 2004]. As such, the meridional propagation directions of GWs show strong seasonal preferences, while zonal propagation directions do not show such characteristics.

As shown in Figure 7, from May to September, most waves propagate northward with the background wind toward the south, which exhibits a quasi-summer feature. From November to March of the next year, the propagation direction exhibits the quasi-winter feature that the majority of waves propagate toward south with the background wind mainly toward the north. In the presence of tidal winds, the meridional component of the wind cannot be ignored. A predominately southward (northward) meridional wind will make the upwardly propagating gravity waves travel northward (southward) during the summer (winter) nighttime. In April, the dominant wave propagation direction turns to east with the background wind turning to west. While in October, both GWs and background wind show no dominant directions. The short transitional period of propagation direction from quasi-summer to quasi-winter is possibly related with local climate, in that both spring and autumn are shorter than the other two seasons. Due to this reason, the features of zonal propagation cannot be fully exhibited. Further combined with Table 1, meridional propagation directions exhibit slightly different features with local latitudes, which might be related with source locations. For example, the predominantly poleward propagating GWs observed over Tanjungsari, Indonesia (7°S), by *Nakamura et al*. [2003] were most probably driven by strong convective sources occurring very closely to the north of Indonesia for most of the year. At midlatitudes [*Wu and Killeen*, 1996; *Walterscheid et al*., 1999; *Hecht et al*., 2001; *Stockwell and Lowe*, 2001a; *Ejiri et al*., 2003; *Nakamura et al*., 2003; *Li et al*., 2011a], the preference of poleward wave motions in summer was mainly due to convective sources near the equator, while strong equatorward wave motions were likely caused by terrain-induced sources and climatic conditions at middle and high latitudes.

The Doppler shifting by background wind also affects the GW propagation direction as described by

$$\omega_i = \omega_o - kv, \tag{13}$$

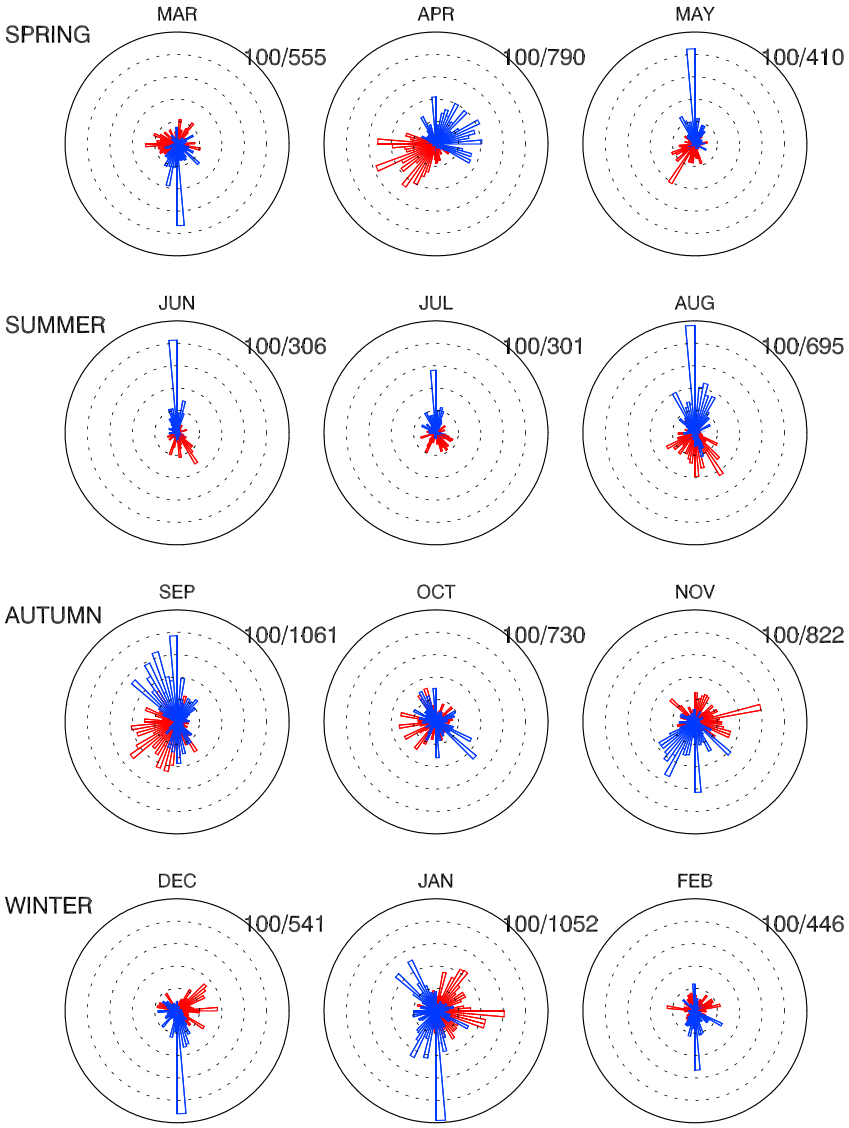

Figure 7. Histograms of GW propagation direction (blue) and wind direction (red) for each month at every season.

where ω_o is the wave frequency relative to the ground and v is the background wind in the GW propagation direction. Figure 8 shows the angle between each GW propagation direction and wind direction. The distribution of waves is tightly clustered approximately 180°. More than 40% of GWs are in the 30° sector centered on 180°, approximately 78% of GWs are in the 60° sector, and approximately 90% of GWs are in the opposite hemisphere relative to the local background wind directions. It is also noticed that the observed phase speeds in the same direction of the background wind are much larger compared to the waves against the mean wind. Combined with Figure 7, these features are consistent throughout the whole year and independent of GW characteristics. This indicates that the background wind strongly impacts GW propagation direction through Doppler shifting. *Li et al.* [2011a] proposed that the cancellation factor *CF* is the main effect on GW propagation direction due to Doppler shifting. However, we think that the CF mainly limits the GW's spectrum window observed by the imager due to the thickness of the airglow layer and that wave breaking is another important effect. Any GWs when propagating along the background wind will break down more easily due to the dynamic or convective instability. Therefore, fewer waves propagating along the mean flow are observed by the airglow imager. It is consistent with the early observation by MF radar [e.g., *Fritts and Vincent*, 1987], suggesting the strong modulation of GWs by the background wind.

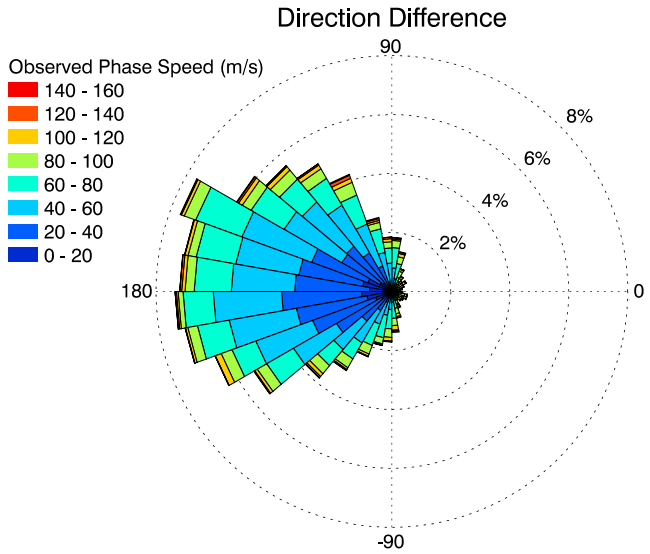

Figure 8. Distribution of the angle between GW propagation direction and background wind for all observed waves. The numbers on the circle indicate percentage of total waves. The majority of waves propagate against the background wind.

As shown in Figure 7, it is also noticed that the wave directionality in April is on average rather than smooth, while in most other months there are large spikes in their main directions. April is the transitional period of propagation direction, so the wave locations are scattered in many directions. Thus, in the influences of the wave source locations and Doppler shifting, the wave directionality is on average rather than smooth in April, vice versa.

Figure 9 shows GW propagation characteristic in January 2006, compared with other years. Figure 9 (left) shows that 1051 GWs wave events are detected in January and most of them propagate southward. Among 367 wave events, which were distributed in the 30° sector centered on south direction in all observed Januaries, 201 wave events are contributed by January 2006 as shown in Figure 9 (left and middle). In other words, a great majority (almost 60%) of GWs travel in this 30° sector during January 2006, while the GW propagation direction exhibits a scattered westward distribution during January except 2006. These features are likely related with stratospheric sudden warming (SSW). A very strong and major Arctic SSW started on 21 January 2006, with which we divided into two durations are shown in Figure 10. The predominantly southward propagation feature faded away after SSW started. This phenomenon is very interesting and needs further analysis with multiple data sets and model simulations to characterize the detailed mechanism.

3.2. Momentum Flux

Figure 11 shows the monthly mean GW momentum fluxes with corresponding monthly mean background wind in the airglow layer at midlatitude Yucca Ridge Field Station. The magnitude is on the order of 10 $m^2 s^{-2}$. The monthly mean of zonal momentum flux shows intraseasonal variation, while the monthly mean

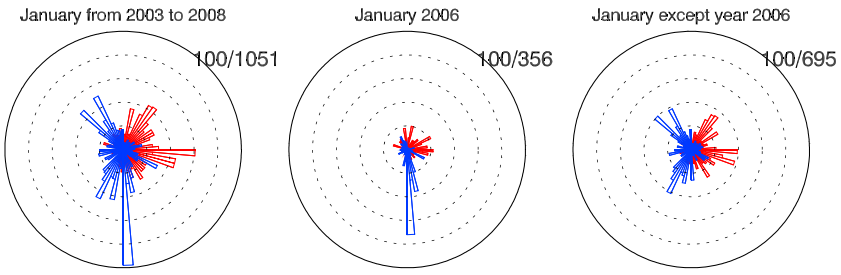

Figure 9. Distributions of GW propagation direction (blue) and wind direction (red) for January (left) from 2003 to 2008, (middle) only 2006, (right) except 2006.

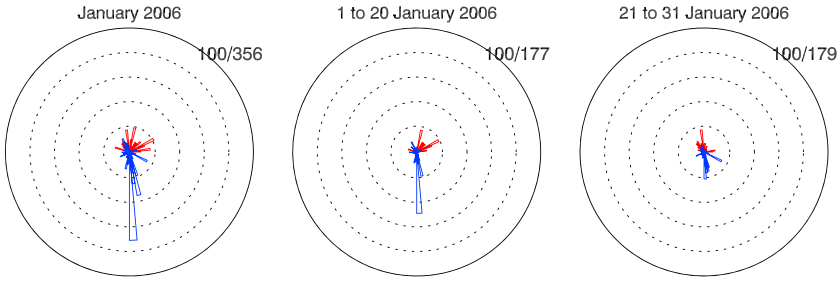

Figure 10. Distributions of GW propagation direction (blue) and wind direction (red) for (left) January 2006, (middle) 1 to 20 January 2006, and (right) 21 to 31 January 2006.

meridional flux shows more prominent annual variation. The meridional wind and momentum flux are clearly anticorrelated. As for GW propagation direction, the monthly mean zonal and meridional GW momentum fluxes also tend to be anticorrelated with the background wind, which is consistent with previous results [*Tang et al.*, 2005; *Suzuki et al.*, 2007; *Gardner and Liu*, 2007; *Li et al.*, 2011a]. The variation of meridional momentum flux shows higher correlation with the variation of meridional mean flow than the zonal correlation. The correlation coefficient between the monthly mean meridional momentum flux and related meridional wind is −0.71, while the correlation coefficient of the zonal component is only −0.46. The opposite trend was observed at low-latitude Maui [*Li et al.*, 2011a]. This difference might be related to the relative location between the wave source and observed station.

Figure 12 shows the mean zonal and meridional momentum fluxes and wind distributions as a function of universal time (UT) and month. The magnitude of meridional momentum flux is obviously larger than the zonal component. The zonal momentum flux shows a clear semiannual variation with a peak of eastward momentum flux at the solstices and westward momentum flux around the equinoxes. In the meridional

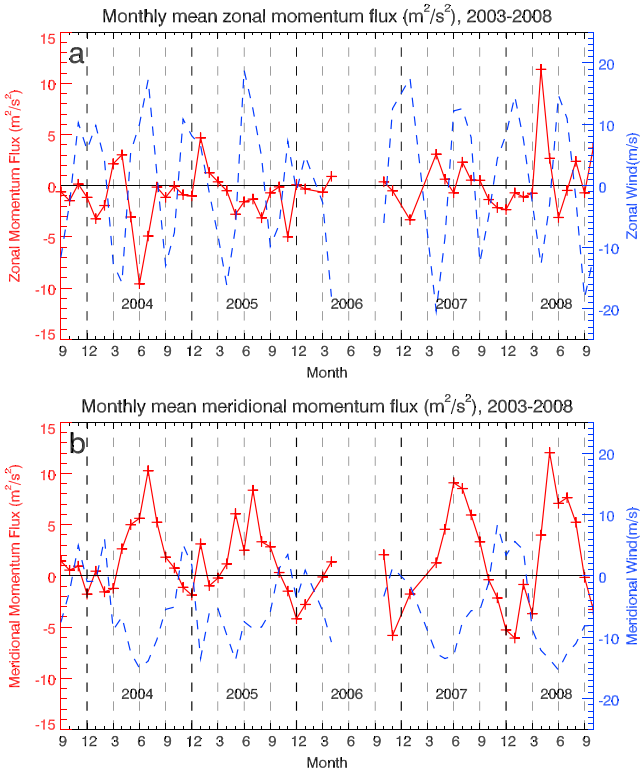

Figure 11. Curves of monthly mean (a) zonal and (b) meridional momentum fluxes (red) and zonal and meridional winds (blue) along time series. The plus signs indicate monthly mean momentum fluxes.

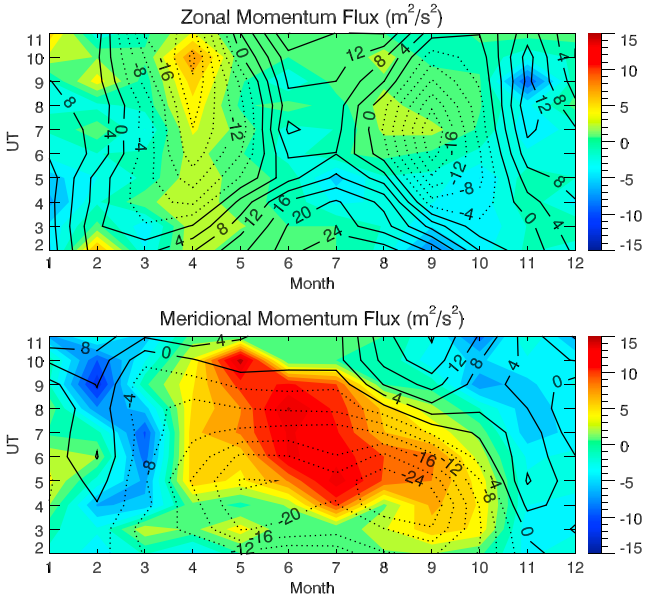

Figure 12. Mean zonal and meridional momentum flux distributions along month and UT with corresponding wind component contours. The unit for wind speed is m s^{-1}. The solid lines indicate that wind speeds are positive, and the dotted lines indicate that wind speeds are negative.

direction, the momentum fluxes are mainly northward in the summer and southward in the winter. The momentum flux is strongly anticorrelated with the background wind. Thus, the mean flow is suppressed as GWs are dissipated or break with momentum and energy deposition in the mesopause region. The early observations of GW momentum flux by MF radar [*Fritts and Vincent*, 1987] also showed clear anticorrelation of GW momentum flux with the mean wind, suggesting the strong modulation of GWs by the mean wind. Therefore, although CF may still affect the observation, our discussion on the mean wind filtering of GWs is still valid.

We extracted the diurnal and semidiurnal tidal components from the wind, as shown in Figure 13. In the zonal component, the momentum flux is 180° out of phase with the tides, while in the meridional component, the

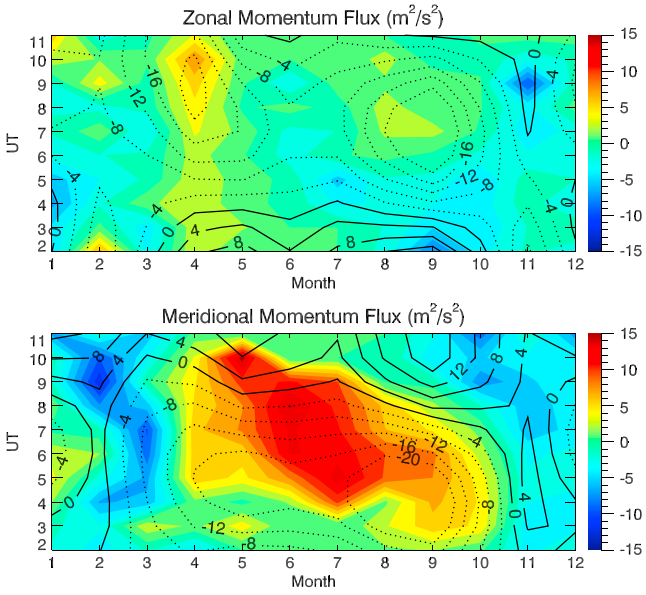

Figure 13. Same as Figure 12 except using extracted diurnal and semidiurnal tidal wind. The unit for wind speed is m s^{-1}. The solid lines indicate that wind speeds are positive, and the dotted lines indicate that wind speeds are negative.

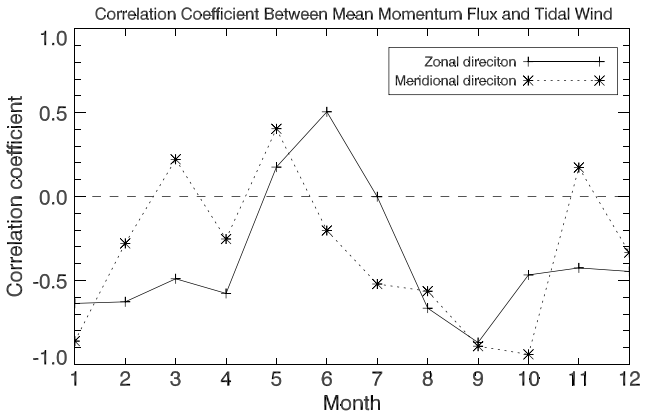

Figure 14. The curves of correlation coefficient between mean momentum flux and tidal wind. The plus signs linked with solid line indicate correlation coefficients for zonal direction, and the asterisks linked with dotted line indicate correlation coefficients for meridional direction.

maximum momentum flux lags the maximum southward tidal wind by ~2–6h. *Fritts and Vincent* [1987] calculated the time difference to be approximately 2 h. *Liu et al.* [2013] reported that the meridional momentum flux and the diurnal tide are approximately 90° out of phase (~6 h). Likewise, the phase of momentum flux also shows seasonal variation with tides. The curves of correlation coefficient between mean momentum flux and tides are shown in Figure 14. The limited number of hourly means momentum fluxes each month introduced large errors when calculating correlation coefficients. However, the curves still exhibit significant features. In the zonal direction, they show strong seasonal variation with weak anticorrelation in summer and strong anticorrelation happens in spring and autumn. In the meridional direction, weak anticorrelation happens in spring and strong anticorrelation in January, September, and October. *Watanabe and Miyahara* [2009] also found that the diurnal tide is amplified (suppressed) during equinoxes (solstices) by GWs using a GW-resolving GCM (general circulation model) to quantify GW forcing on the migrating diurnal tide. These features may be related with the intensity and phase of tides and need further study.

4. Summary

The all-sky OH airglow images observed from 2003 to 2009 at Yucca Ridge Field Station are used to study the high-frequency quasi-monochromatic GW characteristics. The typical horizontal wavelengths and apparent phase speeds are 20–40 km and 30–70 m s^{-1}, respectively. These are consistent with previous studies. The intrinsic periods of GWs cluster approximately 4–10 min. It indicates that many of them are evanescent by assuming climatology of the static stability in OH airglow layer. For the GWs with intrinsic period larger than 5 min, the number of wave events decreases rapidly as the wave period increases.

GW occurrence frequency exhibits a clear semiannual variation with solstitial maxima and equinoctial minima. The seasonal variations of background wind, temperature, and even tides are similar to GW occurrence frequency. This phenomenon suggests that they may be the factors affecting GW activity.

Observed GWs tend to propagate against the background wind except in October and mainly along the meridional direction. It was proposed that wave propagation directions are mainly affected by mean wind filtering, relative location to the wave sources and wave ducting processes. Recently, the Doppler shifting is also examined on the distribution of wave propagation directions.

The mostly southward propagation direction was clearly observed only before 21 January 2006 when a major SSW was onset, and faded out afterward, suggesting strong correlation with the SSW in January 2006.

The estimated momentum fluxes with magnitude of 1–15 $m^2 s^{-2}$ are strongly anticorrelated with the background wind and also modulated strongly by diurnal and semidiurnal tides. For the zonal component, the momentum flux is 180° out of phase with the tides, while the maximum meridional momentum flux lags the maximum southward tidal wind by ~2–6h. Their anticorrelations are the weakest during summer. This also indicates that the tide is possibly amplified (suppressed) during equinoxes (solstices) by GWs [*Watanabe and Miyahara*, 2009].

Acknowledgments
This work was carried out at the University of Science and Technology of China, with support from the National Natural Science Foundation of China grants (41025016, 41127901, 41225017, 41074108, and 41121003), the National Basic Research Program of China grant 2012CB825605, the Chinese Academy of Sciences Key Research Program KZZD-EW-01, and the Fundamental Research Funds for the Central Universities. The geophysical data, such as Ap index, were downloaded from the NOAA National Geophysical Data Center (NGGC), Boulder, Colorado.

Robert Lysak thanks the reviewers for their assistance in evaluating this paper.

References

Alexander, M. J. (1998), Interpretations of observed climatological patterns in stratospheric gravity wave variance, *J. Geophys. Res.*, *103*, 8627–8640.

Coble, M. R., G. C. Papen, and C. S. Gardner (1998), Computing two-dimensional unambiguous horizontal wavenumber spectra from OH airglow images, *IEEE Trans. Geosci. Remote Sens.*, *36*, 368–382.

Dou, X., T. Li, Y. Tang, J. Yue, T. Nakamura, X. Xue, B. P. Williams, and C.-Y. She (2010), Variability of gravity wave occurrence frequency and propagation direction in the upper mesosphere observed by the OH imager in Northern Colorado, *J. Atmos. Sol. Terr. Phys.*, *72*(5–6), 457–462, doi:10.1016/j.jastp.2010.01.002.

Ejiri, M., K. Shiokawa, T. Ogawa, K. Igarashi, T. Nakamura, and T. Tsuda (2003), Statistical study of short-period gravity waves in OH and OI nightglow images at two separated sites, *J. Geophys. Res.*, *108*(D21), 4679, doi:10.1029/2002JD002795.

Fritts, D. C. (1984), Gravity wave saturation in the middle atmosphere: A review of theory and observations, *Rev. Geophys.*, *22*(3), 275–308, doi:10.1029/RG022i003p00275.

Fritts, D. C., and M. J. Alexander (2003), Gravity wave dynamics and effects in the middle atmosphere, *Rev. Geophys.*, *41*(1), 1003, doi:10.1029/2001RG000106.

Fritts, D. C., and P. K. Rastogi (1985), Convective and dynamical instabilities due to gravity wave motions in the lower and middle atmosphere: Theory and observations, *Radio Sci.*, *20*(6), 1247–1277, doi:10.1029/RS020i006p01247.

Fritts, D. C., and R. A. Vincent (1987), Mesospheric momentum flux studies at Adelaide, Australia: Observations and a gravity wave–tidal interaction model, *J. Atmos. Sci.*, *44*(3), 605–619.

Fritts, D. C., and D.-Y. Wang (1991), Doppler-shifting effects on frequency spectra of gravity waves observed near the summer mesopause at high latitude, *J. Atmos. Sci.*, *48*(13), 1535–1544, doi:10.1175/1520-0469(1991)048<1535:DSEOFS>2.0.CO;2.

Garcia, F. J., M. J. Taylor, and M. C. Kelley (1997), Two-dimensional spectral analysis of mesospheric airglow image data, *Appl. Opt.*, *36*, 7374–7385.

Gardner, C. S. and A. Z. Liu (2007), Seasonal variations of the vertical fluxes of heat and horizontal momentum in the mesopause region at Starfire Optical Range, New Mexico, *J. Geophys. Res. 112*, D09113, doi:10.1029/2005JD006179.

Hamilton, K. (1996), Comprehensive meteorological modeling of the middle atmosphere, *J. Atmos. Terr. Phys.*, *58*, 1591–1627.

Hecht, J. H., R. L. Walterscheid, M. P. Hickey, and S. J. Franke (2001), Climatology and modeling of quasi-monochromatic atmospheric gravity waves observed over Urbana, Illinois, *J. Geophys. Res.*, *106*, 5181–5195, doi:10.1029/2000JD900722.

Hecht, J. H., A. Z. Liu, R. L. Walterscheid, and R. J. Rudy (2005), Maui Mesosphere and Lower Thermosphere (Maui MALT) observations of the evolution of Kelvin-Helmholtz billows formed near 86 km altitude, *J. Geophys. Res.*, *110*, D09S10, doi:10.1029/2003JD003908.

Hu, X., A. Z. Liu, C. S. Gardner, and G. R. Swenson (2002), Characteristics of quasi-monochromatic gravity waves observed with Na lidar in the mesopause region at Starfire Optical Range, NM, *Geophys. Res. Lett.*, *29*(24), 22–1, doi:10.1029/2002GL014975.

Jacobi, C., C. Arras, D. Kürschner, W. Singer, P. Hoffmann, and D. Keuer (2008), Comparison of mesopause region meteor radar winds, medium frequency radar winds and low frequency drifts over Germany, *Adv. Space Res.*, *43*, 247–252.

Kubota, M., H. Fukunishi, and S. Okano (2001), Characteristics of medium- and large-scale TIDs over Japan derived from OI 630-nm nightglow observation, *Earth Planets Space*, *53*, 741–751.

Lane, T. P. and M. W. Moncrieff (2008), Stratospheric gravity waves generated by multiscale tropical convection, *J. Atmos. Sci.*, *65*, 2598–2614, doi:10.1175/2007JAS2601.1.

Li Q., J. Xu, J. Yue, W. Yuan, and X. Liu (2011), Statistical characteristics of gravity wave activities observed by an OH airglow imager at Xinglong, in northern China, *Ann. Geophys.*, *29*, 1401–1410, doi:10.5194/angeo-29-1401-2011.

Li, T., C. Y. She, B. P. Williams, T. Yuan, R. L. Collins, L. M. Kieffaber, and A. W. Peterson (2005), Concurrent OH imager and sodium temperature/wind lidar observation of localized ripples over northern Colorado, *J. Geophys. Res.*, *110*, D13110, doi:10.1029/2004JD004885.

Li, Z., A. Z. Liu, X. Lu, G. R. Swenson, and S. J. Franke (2011a), Gravity wave characteristics from OH airglow imager over Maui, *J. Geophys. Res.*, *116*, D22115, doi:10.1029/2011JD015870.

Li, Z., A. Z. Liu, S. J. Franke, G. Swenson,and X. Lu (2011b), Gravity wave characteristics observed with airglow imager at the Andes Lidar Observatory, AGU Fall Meeting.Manney,

Liu A. Z., X. Lu, and S. J. Franke (2013), Diurnal variation of gravity wave momentum flux and its forcing on the diurnal tide, *J. Geophys. Res. Atmospheres*, *118*, 1668–1678, doi:10.1029/2012JD018653.

Medeiros, A. F., M. J. Taylor, H. Takahashi, P. P. Batista, and D. Gobbi (2003), An investigation of gravity wave activity in the low-latitude upper mesosphere: Propagation direction and wind filtering, *J. Geophys. Res.*, *108*(D14), 4411, doi:10.1029/2002JD002593.

Ming, X., and D. Kang (1996), Corrections for frequency, amplitude and phase in a fast Fourier transform of a harmonic signal, *Mech. Syst. Sig. Process.*, *10*, 211–221.

Nakamura, T., T. Tsuda, S. Fukao, A. H. Manson, C. E. Meek, R. A. Vincent, and I. M. Reid (1996), Mesospheric gravity waves at Saskatoon (52°N), Kyoto (35°N), and Adelaide (35°S), *J. Geophys. Res.*, *101*(D3), 7005–7012.

Nakamura, T., A. Higashikawa, T. Tsuda, and Y. Matsushita (1999), Seasonal variations of gravity wave structures in OH airglow with a CCD imager at Shigaraki, *Earth Planets Space*, *51*, 897–906.

Nakamura, T., T. Aono, T. Tsuda, A. Admiranto, E. Achmad, and Suranto (2003), Mesospheric gravity waves over a tropical convective region observed by OH airglow imaging in Indonesia, *Geophys. Res. Lett.*, *30*(17), 1882, doi:10.1029/2003GL017619.

Nakamura, T., T. Fukushima, T. Tsuda, C. Y. She, B. P. Williams, D. Krueger, and W. Lyons (2005), Simultaneous observation of dual-site airglow imagers and a sodium temperature wind lidar, and effect of atmospheric stability on the airglow structure, *Adv. Space Res.*, *35*, 1957–1963, doi:10.1016/j.asr.2005.05.102.

Nielsen, K., M. J. Taylor, R. E. Hibbins, and M. J. Jarvis (2009), Climatology of short-period mesospheric gravity waves over Halley, Antarctica (76°S, 27°W), *J. Atmos. Sol. Terr. Phys.*, *71*, 991–1000, doi:10.1016/j.jastp.2009.04.005.

Picone, J. M., A. E. Hedin, D. P. Drob, and A. C. Aikin (2002), NRLMSISE-00 empirical model of the atmosphere: Statistical comparisons and scientific issues, *J. Geophys. Res.*, *107*(A12), 1468, doi:10.1029/2002JA009430.

Stockwell, R. G., and R. P. Lowe (2001a), Airglow imaging of gravity waves: 1. Results from a small network of OH nightglow scanning imagers, *J. Geophys. Res.*, *106*, 17,185–17,203, doi:10.1029/2001JD900035.

Stockwell, R. G., and R. P. Lowe (2001b), Airglow imaging of gravity waves: 2. Critical layer filtering, *J. Geophys. Res.*, *106*, 17,205–17,220, doi:10.1029/2001JD900036.

Suzuki, S., K. Shiokawa, Y. Otsuka, T. Ogawa, and P. Wilkinson (2004), Statistical characteristics of gravity waves observed by an all-sky imager at Darwin, Australia, *J. Geophys. Res.*, *109*, D20S07, doi:10.1029/2003JD004336.

Suzuki, S., K. Shiokawa, Y. Otsuka, T. Ogawa, M. Kubota, M. Tsutsumi, T. Nakamura, and D. C. Fritts (2007), Gravity wave momentum flux in the upper mesosphere derived from OH airglow imaging measurements, *Earth Planets Space*, *59*, 421–428.

Swenson, G., and A. Liu (1998), A model for calculating acoustic gravity wave energy and momentum flux in the mesosphere from OH airglow, *Geophys. Res. Lett.*, *25*(4), 477–480, doi:10.1029/98GL00132.

Swenson, G., and S. B. Mende (1994), OH emission and gravity waves (including a breaking wave) in all-sky imagery from Bear Lake, UT, *Geophys. Res. Lett.*, *21*, 2239–2242.

Swenson, G., M. Alexander, and R. Haque (2000), Dispersion imposed limits on atmospheric gravity waves in the mesosphere: Observations from OH airglow, *Geophys. Res. Lett.*, *27*(6), 875–878, doi:10.1029/1999GL010738.

Tang, J., F. Kamalabadi, S. Franke, A. Liu, and G. Swenson (2005), Estimation of gravity wave momentum flux with spectroscopic imaging, *IEEE Trans. Geosci. Remote Sens.*, *43*(1), 103–109, doi:10.1109/TGRS.2004.836268.

Taylor, M., E. Ryan, T. Tuan, and R. Edwards (1993), Evidence of preferential directions for gravity wave propagation due to wind filtering in the middle atmosphere, *J. Geophys. Res.*, *98*(A4), 6047–6057, doi:10.1029/92JA02604.

Taylor, M. J., W. R. Pendleton, S. Clark, H. Takahashi, D. Gobbi, and R. A. Goldberg (1997), Image measurements of short-period gravity waves at equatorial latitudes, *J. Geophys. Res.*, *102*, 26,283–26,299, doi:10.1029/96JD03515.

Vincent, R. A. (1984), Gravity-wave motions in the mesosphere, *J. Atmos. Sol. Terr. Phys.*, *46*(2), 119–128.

Walterscheid, R., J. Hecht, R. Vincent, I. Reid, J. Woithe, and M. Hickey (1999), Analysis and interpretation of airglow and radar observations of quasi-monochromatic gravity waves in the upper mesosphere and lower thermosphere over Adelaide, Australia (35°S, 138°E), *J. Atmos. Sol. Terr. Phys.*, *61*(6), 461–478, doi:10.1016/S1364-6826(99)00002-4.

Watanabe, S., and S. Miyahara (2009), Quantification of the gravity wave forcing of the migrating diurnal tide in a gravity wave-resolving general circulation model, *J. Geophys. Res.*, *114*, D07110, doi:10.1029/2008JD011218.

Wu, Q., and T. L. Killeen (1996), Seasonal dependence of mesospheric gravity waves (<100 km) at Peach Mountain Observatory, Michigan, *Geophys. Res. Lett.*, *23*, 2211–2214.